PNAS RESEARCH ARTICLE | IMMUNOLOGY AND INFLAMMATION OPEN ACCESS

The IRG1–itaconate axis protects from cholesterol-induced inflammation and atherosclerosis

Yannick Cyr[a,1], Fazli K. Bozal[a,1], José Gabriel Barcia Durán[a], Alexandra A. C. Newman[a], Letizia Amadori[a], Panagiotis Smyrnis[a], Morgane Gourvest[a], Dayasagar Das[a], Michael Gildea[a], Ravneet Kaur[a], Tracy Zhang[a], Kristin M. Wang[a], Richard Von Itter[a], P. Martin Schlegel[b], Samantha D. Dupuis[a], Bernard F. Sanchez[a], Ann Marie Schmidt[a,c], Edward A. Fisher[a,d], Coen van Solingen[a], Chiara Giannarelli[a,e], and Kathryn J. Moore[a,d,2]

Contributed by Kathryn J. Moore; received January 16, 2024; accepted February 28, 2024; reviewed by Luke A. O'Neill and Neal Silverman

Atherosclerosis is fueled by a failure to resolve lipid-driven inflammation within the vasculature that drives plaque formation. Therapeutic approaches to reverse atherosclerotic inflammation are needed to address the rising global burden of cardiovascular disease (CVD). Recently, metabolites have gained attention for their immunomodulatory properties, including itaconate, which is generated from the tricarboxylic acid-intermediate cis-aconitate by the enzyme Immune Responsive Gene 1 (IRG1/ACOD1). Here, we tested the therapeutic potential of the IRG1–itaconate axis for human atherosclerosis. Using single-cell RNA sequencing (scRNA-seq), we found that *IRG1* is up-regulated in human coronary atherosclerotic lesions compared to patient-matched healthy vasculature, and in mouse models of atherosclerosis, where it is primarily expressed by plaque monocytes, macrophages, and neutrophils. Global or hematopoietic *Irg1*-deficiency in mice increases atherosclerosis burden, plaque macrophage and lipid content, and expression of the proatherosclerotic cytokine interleukin (IL)-1β. Mechanistically, absence of *Irg1* increased macrophage lipid accumulation, and accelerated inflammation via increased neutrophil extracellular trap (NET) formation and NET-priming of the NLRP3-inflammasome in macrophages, resulting in increased IL-1β release. Conversely, supplementation of the *Irg1*–itaconate axis using 4-octyl itaconate (4-OI) beneficially remodeled advanced plaques and reduced lesional IL-1β levels in mice. To investigate the effects of 4-OI in humans, we leveraged an ex vivo systems-immunology approach for CVD drug discovery. Using CyTOF and scRNA-seq of peripheral blood mononuclear cells treated with plasma from CVD patients, we showed that 4-OI attenuates proinflammatory phospho-signaling and mediates anti-inflammatory rewiring of macrophage populations. Our data highlight the relevance of pursuing IRG1–itaconate axis supplementation as a therapeutic approach for atherosclerosis in humans.

atherosclerosis | innate immunity | immunometabolism | macrophage | neutrophil

Significance

Novel therapeutic strategies targeting the inflammatory component of atherosclerotic cardiovascular disease (CVD) are urgently needed. We show that the enzyme immune responsive gene 1 (IRG1) and its immunomodulatory product, itaconate, protect from atherosclerotic inflammation in humans and mice. Using mouse models and human coronary tissues, we show that IRG1 is expressed in atherosclerotic plaques, and its deficiency increases plaque burden. Conversely, supplementing the IRG1–itaconate axis with 4-octyl itaconate induces beneficial remodeling of advanced atherosclerotic plaques in mice and reduces CVD-associated inflammation in human immune cell populations. These findings underscore the therapeutic promise of targeting the IRG1–itaconate pathway for the treatment of CVD.

Cardiovascular diseases (CVD) remain the leading cause of death and are often the result of advanced atherosclerosis, a chronic inflammatory condition stemming from the retention and modification of cholesterol-rich low density lipoproteins (LDL) in the artery wall (1). Therapeutic efforts to reduce atherosclerotic risk have largely focused on lowering plasma levels of LDL cholesterol. Yet, despite achieving target cholesterol levels, many patients remain at high risk of a cardiovascular event due, in part, to residual inflammation, which has prompted the development of orthogonal approaches aimed at promoting inflammation resolution (2).

Chronic activation of innate immune cells, particularly monocytes, macrophages, and neutrophils, contributes to the inflammatory milieu of the atherosclerotic plaque (3, 4). Macrophages recognize and clear atherogenic lipoproteins (e.g., oxidized or aggregated LDL), contributing to both the maintenance of lipid homeostasis in the artery wall and innate immune activation, which results in the production of proinflammatory cytokines [e.g., interleukin (IL)-6, interferons (IFN)], and chemokines (e.g., CCL2, CCL5) (2, 3). Macrophage recognition of oxidized LDL (oxLDL) (5) and cholesterol crystals (CC) (6) also plays important roles in the priming and activation, respectively, of the NLRP3 inflammasome, which regulates the release of the proatherosclerotic cytokine IL-1β. Neutrophils also contribute to plaque inflammation by elaborating reactive oxygen species (ROS), neutrophil extracellular traps (NETs), and proteases that activate surrounding immune and endothelial cells and degrade extracellular matrix, enabling further leukocyte infiltration (4, 7). These mechanisms create a feed-forward loop wherein lipid-driven inflammatory responses fuel maladaptive inflammation (3). Failure of innate and adaptive immune cells to resolve this inflammation leads to plaque progression, and ultimately plaque rupture and its sequelae, myocardial infarction or stroke.

Reviewers: L.A.O., The University of Dublin Trinity College; and N.S., University of Massachusetts Medical School.

Competing interest statement: K.J.M. is on the scientific advisory Board of Beren Therapeutics and Bitterroot Bio. K.J.M. and A.M.S. have patents and patent applications through NYU Grossman School of Medicine that have been submitted/published and that are not related to the work detailed in this manuscript. The other authors declare no conflict of interest.

[1]Y.C. and F.K.B. contributed equally to this work.

[2]To whom correspondence may be addressed. Email: kathryn.moore@nyulangone.org.

This article contains supporting information online at https://www.pnas.org/lookup/suppl/doi:10.1073/pnas.2400675121/-/DCSupplemental.

Published April 2, 2024.

Cellular metabolism intrinsically fuels the inflammatory function of immune cells. Itaconate is a tricarboxylic acid (TCA) cycle-derived metabolite produced from cis-aconitate by the enzyme cis-aconitate decarboxylase (ACOD1/IRG1; gene *Irg1*), which is markedly up-regulated in classically activated macrophages (8). Itaconate accumulates rapidly following macrophage activation with bacterial lipopolysaccharide (LPS) and can reduce inflammation by inhibiting glycolysis, succinate dehydrogenase, ROS, type I IFN production, and IL-1β secretion (8–10). Itaconate's anti-inflammatory effects have been attributed to alkylation of kelch-like ECH-associated protein 1 (KEAP1) leading to activation of antioxidant transcription factor nuclear factor erythroid-related factor 2 (NRF2) (11), modification of NLPR3 that prevents its oligomerization and inflammasome activation (12), induction of activating transcription factor 3 (ATF3) to inhibit IκBζ activation (13), as well as alkylation and inhibition of enzymes involved in glycolysis (9, 14). Accordingly, *Irg1*-deficient ($Irg1^{-/-}$) mice have heightened immune responses and increased secretion of proinflammatory cytokines (IL-1β, IL-6, IL-12, IL-18) in response to LPS stimulation (15). Single nucleotide polymorphisms (SNPs) affecting the expression of *IRG1* alter the expression of IL-6 and TNFα, and lactate production (16), highlighting the physiological relevance of this pathway in humans. In fact, the immunomodulatory properties of itaconate and its synthetic derivative 4-octyl itaconate (4-OI) are being actively tested in infectious disease settings (10, 17). Administration of 4-OI significantly reduces inflammatory cytokine release and mortality in mice treated with LPS (14) and prevents *Mycobacterium tuberculosis*-induced mortality (18). Mechanistically, 4-OI has been shown to stabilize the antioxidant and anti-inflammatory transcription factors NRF2 and Activating Transcription Factor 3 (ATF3), leading to induction of NRF2-target genes such as *Hmox1* and *Nqo1*, which decrease cellular ROS and suppress HIF-α (8, 9, 11, 13–15, 18–21). Notably, many of these processes are dysregulated in atherosclerosis, and the variant rs73537762-C in *IRG1* has been associated with decreased cholesteryl ester levels in genome-wide association studies (GWAS) (22). However, the regulation of IRG1 and its downstream metabolites in the chronic inflammatory setting of the atherosclerotic plaque remain poorly understood.

Here, we show that *IRG1* is up-regulated in myeloid cells of human and mouse atherosclerotic plaques, yet its expression wanes with disease progression. Loss-of-function studies in mouse models of atherosclerosis demonstrate that global and hematopoietic *Irg1*-deficiency increase atherosclerotic burden, plaque lipid content, and indices of plaque instability. Mechanistically, *Irg1* deficiency increases NET formation, which acts as a priming signal for the NLRP3 inflammasome in macrophages. In turn, $Irg1^{-/-}$ macrophages display elevated NET-induced inflammasome priming and activation, resulting in enhanced production of IL-1β, a potent proatherosclerotic cytokine (23). Together, our data show that absence of *Irg1* fuels a feed-forward proinflammatory cross talk between neutrophils and macrophages. In vivo, therapeutic administration of the itaconate-derivative 4-OI induced anti-inflammatory remodeling of advanced atherosclerotic plaques and plaque regression. At single-cell resolution in a human model of CVD-related systemic inflammation, 4-OI supplementation attenuated the rapid proinflammatory signaling cascade induced by treatment of peripheral blood mononuclear cells (PBMCs) with CVD patient plasma, decreased neutrophil degranulation gene signatures, and bolstered antioxidant and anti-inflammatory gene pathways in macrophages. Collectively, our data identify the IRG1–itaconate axis as an important regulator of atherosclerotic inflammation that can be therapeutically harnessed in humans and mice.

Results

IRG1 Is Expressed in Human and Mouse Atherosclerotic Plaques. To investigate the expression of *IRG1* in human atherosclerosis, we performed single-cell RNA sequencing (scRNA-seq) of human coronary fibroatheromas (FA, n = 2) and paired coronary adaptive intimal thickening (AIT) from the same patients (n = 2, Fig. 1*A*). *IRG1* transcript levels were enriched in FA compared to nondiseased AIT, and its expression was predominantly localized to immune cells (Fig. 1*A*). *IRG1* was most highly expressed by myeloid cells, which amounted to over 20% of all immune cells within the immune cell compartment of coronary plaques (*SI Appendix*, Fig. S1 *A* and *B*), and particularly in monocytes and macrophages (Fig. 1 *B*–*D*). This was confirmed by immunostaining of human coronary arteries (Fig. 1*E* and *SI Appendix*, Fig. S1*C*) and carotid artery plaques (*SI Appendix*, Fig. S1*D*), which showed colocalization of IRG1 and the monocyte/macrophage marker CD68.

To further investigate how *Irg1* expression is modulated during atherogenesis, we fed $Ldlr^{-/-}$ mice a western diet (WD) for 8, 12, or 16 wk to simulate early, moderate and advanced atherosclerosis. We performed scRNA-seq of $CD45^+$ cells isolated from the aortic arch (an area of plaque accumulation) of mice with advanced atherosclerosis (16 wk WD), and detected all major immune cell types (*SI Appendix*, Fig. S1*E*). We confirmed that *Irg1* was highly expressed in myeloid cells within mouse atherosclerotic tissue, particularly monocytes and neutrophils (Fig. 1*F*), but not adaptive immune cells. Interestingly, although *Irg1* transcript levels were high in monocytes, which are associated with active infiltration of the arterial intima and acute inflammation, it was lower in longer-lived plaque macrophages (Fig. 1*F*), indicating that its expression becomes limited. To confirm our transcriptomic analyses, we performed IRG1 immunostaining of cross-sections of the aortic root of $Ldlr^{-/-}$ mice. Within the plaque, IRG1 staining strongly colocalized with the monocyte/macrophage marker CD68, and to a lesser extent with the neutrophil marker Ly6G (Fig. 1*G*). Notably, we observed that the proportion of $IRG1^+$ cells within the plaque was highest in $Ldlr^{-/-}$ mice with early atherosclerosis (8 wk WD), but declined with continued WD feeding, suggesting that this anti-inflammatory mechanism wanes with plaque progression (Fig. 1*H*). To investigate the transcriptomic changes associated with expression of *Irg1*, we built a differential gene expression matrix that compared *Irg1*-expressing ($Irg1^+$) and nonexpressing ($Irg1^-$) cells within each myeloid subcluster from our scRNA-seq analysis of mouse plaques (Fig. 1*I*). Using this approach, we observed pronounced transcriptional differences associated with *Irg1* expression within the monocyte, macrophage and neutrophil clusters (Fig. 1*I*). Ingenuity Pathway Analysis of the 526 genes that were up- and 707 genes down-regulated in *Irg1* expressing vs. nonexpressing myeloid cells (P-adj < 0.05, $-0.5 < \text{Log}_2$ fold change > 0.5) revealed a transcriptional pattern indicative of increased inflammatory activity and mitochondrial dysfunction in $Irg1^+$ cells (Fig. 1*J*). Notably, $Irg1^+$ cells showed down-regulated expression of *Apoe*, *Trem2* and *Lpl*, which are genes characteristic of the lipid-handling properties of macrophage foam cells (Fig. 1*J*). Additionally, endogenous ligands predicted to be upstream of these transcriptional changes included proatherosclerotic lipid mediators (24) generated through mitochondrial metabolism (Fig. 1*J*). These data implicate *Irg1* in metabolic reprograming of myeloid cells within the plaque.

***Irg1*-Deficiency Aggravates Atherosclerosis Development.** To test how atherogenic lipoproteins alter the metabolic state of macrophages, we treated mouse bone marrow-derived macrophages (BMDMs), with aggregated (ag)LDL or oxLDL, and performed

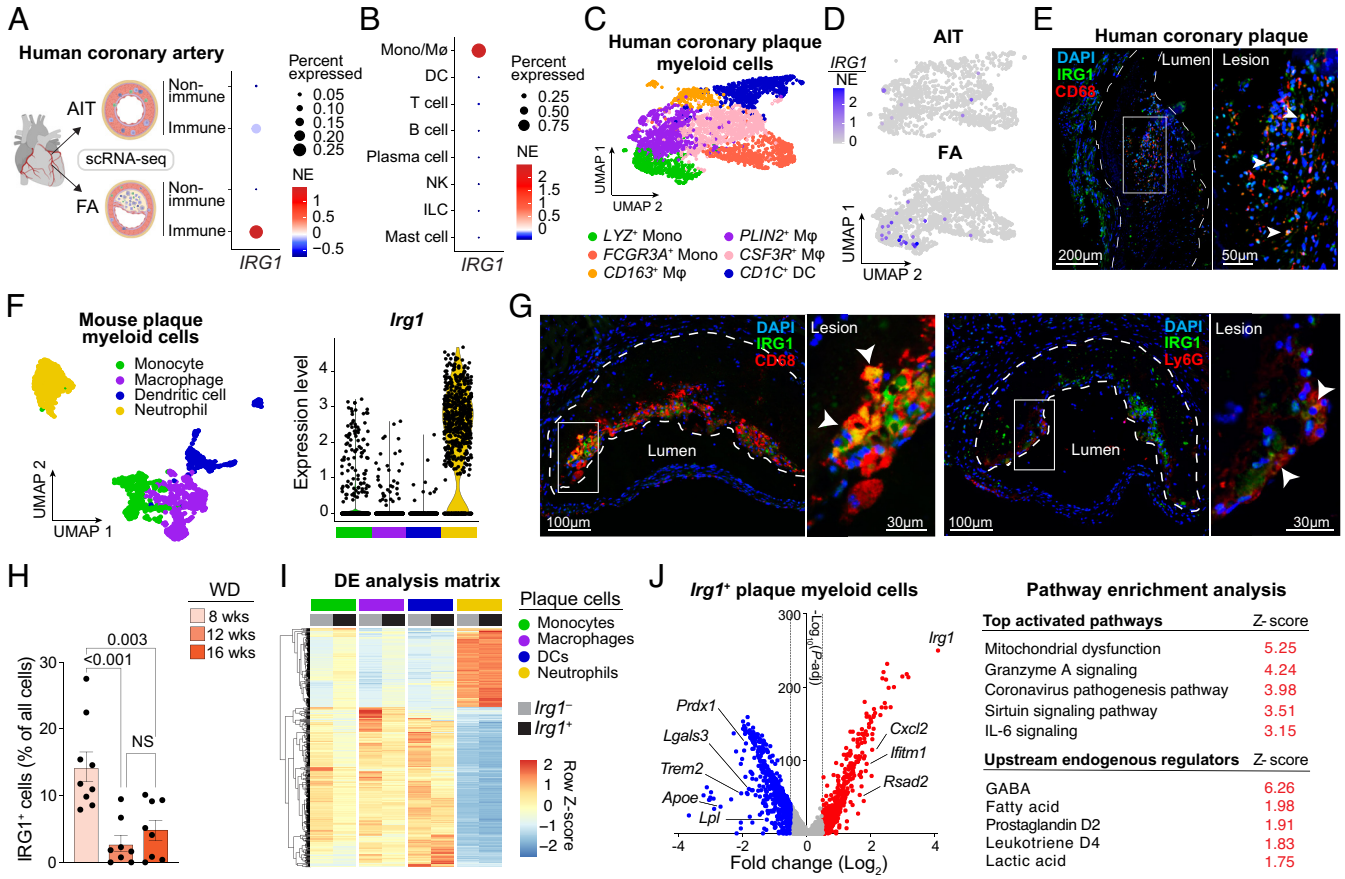

Fig. 1. IRG1 is expressed in plaque immune cells and wanes with atherosclerosis progression in humans and mice. (*A–D*) Experimental outline of scRNA-seq of human coronary fibroatheroma (FA) or patient-matched regions of adaptive intimal thickening (AIT) (*A*, *Left*). Average *IRG1* normalized expression (NE) in immune and nonimmune populations by disease pathology (*A*, *Right*). Average *IRG1* NE by immune cell type (*B*). Uniform Manifold Approximation and Projection (UMAP) visualization of myeloid cells from human coronary plaques stratified by cell type (*C*) or *IRG1* NE (*D*), n = 3,556 cells; Mono/Mø, monocyte/macrophage; DC, dendritic cell; NK, natural killer; ILC, innate lymphoid cell. (*E*) Immunofluorescent staining showing colocalization (arrows) of CD68 and IRG1 in human coronary plaque, (*F*) UMAP visualization of myeloid cell clusters from scRNA-seq of the aortic arch of male and female *Ldlr*$^{-/-}$ mice fed a WD for 16 wk (*Left*), with violin plot showing *Irg1* expression (*Right*) (n = 8,669 cells). (*G*) Immunofluorescent staining for IRG1 and Mono/Mø (CD68, *Left*) or neutrophils (Ly6G, *Right*) in aortic root plaques of *Ldlr*$^{-/-}$ mice fed WD (12 wk). Arrows indicate staining colocalization. (*H*) Quantification of plaque IRG1^{+} cells along the aortic root of WD-fed *Ldlr*$^{-/-}$ male mice. *P*-values calculated by one-way ANOVA with Tukey's multiple-comparison test. (*I*) Normalized gene expression matrix showing the 500 most DEG between *Irg1* expressing (*Irg1*$^{+}$) and nonexpressing (*Irg1*$^{-}$) myeloid cells by cluster. (*J*) Volcano plot of genes differentially expressed between *Irg1*$^{+}$ and *Irg1*$^{-}$ myeloid cells, with predicted pathways and upstream regulators. Dashed lines indicate fold change $|\text{Log}_2| \pm 0.5$. (*A–D*) n = 2 patients, matched for AIT and FA; (*F*, *I*, and *J*) n = 10; 5 mice/sex, (*H*) n = 8 to 9 mice/group.

targeted liquid chromatography and tandem mass spectrometry (LC–MS) to identify polar intracellular metabolites. We observed significant differences in the accumulation of 29 metabolites within agLDL- or oxLDL-treated cells, including itaconate (Fig. 2*A*). Using a neat standard curve in LC–MS, we confirmed that BMDM treated with agLDL and oxLDL accumulated itaconate intracellularly (Fig. 2*B*), and observed twofold and eightfold increases, respectively, in *Irg1* mRNA by quantitative RT-PCR (Fig. 2*C*). Similar findings were observed in human THP1 macrophages and mouse neutrophils (*SI Appendix*, Fig. S2 *A* and *B*).

To test the role of the IRG1–itaconate axis in limiting atherosclerotic inflammation, we induced hypercholesterolemia in wild-type (WT) and *Irg1*$^{-/-}$ mice using an adeno-associated virus (AAV) vector bearing gain-of-function murine PCSK9-D377Y, coupled with WD feeding as we described (25, 26). Immunostaining of cross-sections of the aortic root taken after 12 wk of WD feeding confirmed the absence of IRG1 expression in plaques of *Irg1*$^{-/-}$ mice (Fig. 2*D*), and revealed greater plaque burden throughout the length of the aortic root compared to WT mice (Fig. 2*E*), in the absence of differences in plasma cholesterol levels or body weight (*SI Appendix*, Fig. S2*C*). Furthermore, *Irg1*$^{-/-}$ plaques showed higher levels of immunostaining for the macrophage marker CD68 (Fig. 2*F*) and BODIPY-staining of neutral lipid (Fig. 2*G*), even after correcting for plaque size. Together, these data suggest increased accumulation of macrophage foam cells and plaque progression in *Irg1*-deficient mice.

To examine how *Irg1*-deficiency alters the transcriptional signatures and dynamics of immune cell populations in plaque, we performed scRNA-seq of CD45^{+} cells isolated from the aortic arches of WT or *Irg1*$^{-/-}$ atherosclerotic mice. This approach yielded 6,022 single leukocytes belonging to 16 immune cell types as determined by Louvain clustering (Fig. 2*H*). Of the eight myeloid clusters identified, *Lyve1*$^{+}$ and *Trem2*$^{+}$ macrophages constituted the two most abundant subpopulations captured, amounting to ~50% of innate immune cells found within atherosclerotic tissue irrespective of genotype. *Lyve1* is recognized as a marker of anti-inflammatory, resident macrophages (27), while *Trem2* has been identified as a regulator of foamy macrophage differentiation specifically in the context of increased atherosclerotic burden (28). In the absence of *Irg1*, *Lyve1*$^{+}$ macrophages appeared decreased and *Trem2*$^{+}$ macrophages were significantly more abundant compared to WT plaques ($P = 7 \times 10^{-3}$; Fig. 2*I*). Differential expression analysis revealed that the majority of gene expression changes detected in *Irg1*$^{-/-}$ plaques were found in *Lyve1*$^{+}$ macrophages or neutrophils (Fig. 2*J*). Canonical pathway analyses revealed that compared to their WT counterparts, *Irg1*$^{-/-}$ *Lyve1*$^{+}$ macrophages

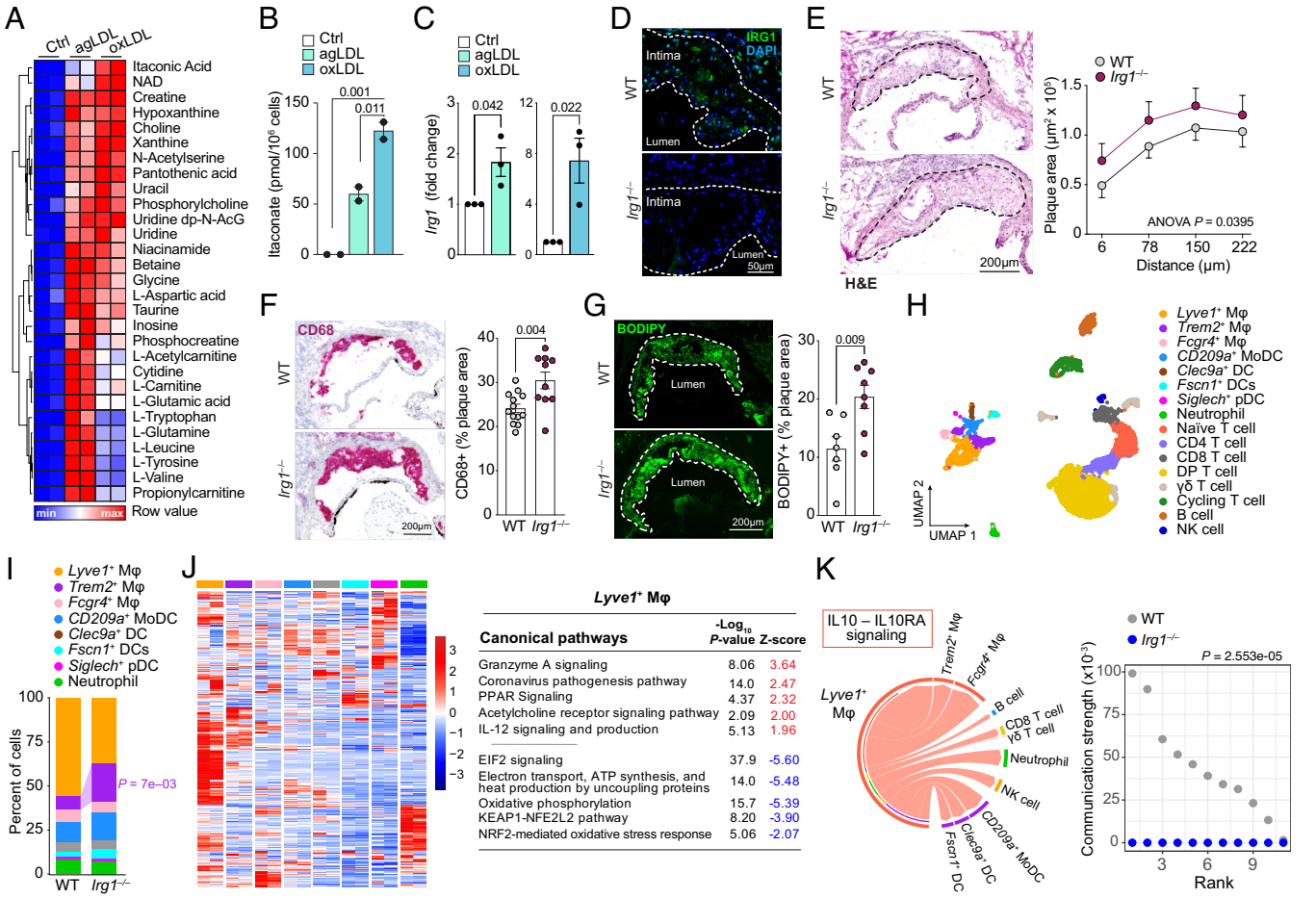

Fig. 2. Genetic deletion of *Irg1* aggravates atherosclerosis development. (*A*) Targeted metabolomic measurements and (*B*) absolute quantification of itaconate in BMDMs treated with aggregated (ag)LDL or oxidized (ox)LDL (50 μg/mL, 24 h). (*C*) *Irg1* mRNA levels in BMDMs stimulated with agLDL and oxLDL for 8 h. (*D–G*) Aortic root plaques of male WT and *Irg1*$^{-/-}$ mice treated with PCSK9-AAV and WD (12 wk), showing representative staining and quantification of IRG1 (*D*), H&E stain and plaque area through the aortic root (*E*), CD68 (*F*), and BODIPY neutral lipid stain (*G*). (*H–K*) scRNA-seq analysis of CD45^{+} cells isolated from the aortic arch of WT and *Irg1*$^{-/-}$ male mice treated with PCSK9-AAV and WD (16 wk) visualized by UMAP (*H*); bar plot showing frequency of myeloid cell subpopulations (*I*); Differential gene expression in myeloid subpopulations between WT and *Irg1*$^{-/-}$ mice (*Left*), with predicted canonical pathways altered in *Irg1*$^{-/-}$ vs. WT *Lyve1*$^{+}$ Mø (*J*); and chord diagram of predicted IL10–IL10ra signaling in WT *Lyve1*$^{+}$ Mø (*Left*) and communication strength (*Right*) (*K*). *P*-values calculated by (*B*) one ANOVA with Tukey's multiple-comparison test; (*C*, *F*, *G*, and *I*) Student's *t* test; (*E*) two-way ANOVA; (*K*) Kolmogorov–Smirnov test. (*B*) n = 2 mice/group; (*C*) n = 3 mice/group; (*D–F*) n = 10 to 14 mice/group; (*G*) n = 7 to 8 mice/group; and (*H*) n = 5 mice/group.

displayed a proinflammatory transcriptional program, as evidenced by the emergence of terms associated with T cell activation, such as Granzyme A and IL-12 signaling, and the concomitant downregulation of oxidative phosphorylation and NRF2-mediated signaling (Fig. 2*J*). Using CellChat, a computational tool that infers cell–cell interactions based on gene expression of receptor–ligand pairs from scRNA-seq datasets, we found that WT *Lyve1*$^{+}$ macrophages engaged in immune dampening IL-10 signaling with multiple lymphoid and myeloid cell clusters, but this signaling was absent in *Irg1*$^{-/-}$ *Lyve1*$^{+}$ macrophages ($P = 2.55 \times 10^{-5}$; Fig. 2*K*) (29). These data suggest that the loss of *Irg1* enhances the accumulation lipid-loaded macrophages and promotes a proinflammatory transcriptional program in resident macrophages, which may accelerate atherosclerosis.

Hematopoietic *Irg1* Expression Protects against Atherosclerosis Development. To confirm that *Irg1* expression within myeloid cells protects against atherosclerosis development, we reconstituted lethally irradiated *Ldlr*$^{-/-}$ mice with bone marrow from *Irg1*$^{-/-}$ (*Irg1*$^{-/-}$ → *Ldlr*$^{-/-}$) or WT (WT → *Ldlr*$^{-/-}$) mice, and after 6 wk of recovery, fed them a WD for 12 wk. Similar to mice with global *Irg1*-deficiency, male and female chimeric *Irg1*$^{-/-}$ → *Ldlr*$^{-/-}$ mice showed greater plaque burden throughout the length of the aortic root compared to WT → *Ldlr*$^{-/-}$ mice of the same sex (Fig. 3*A*). This was accompanied by higher plaque macrophage and lipid content in *Irg1*$^{-/-}$ → *Ldlr*$^{-/-}$ mice, even after correction for plaque size (Fig. 3*B*), despite similar body weights and serum cholesterol levels to WT → *Ldlr*$^{-/-}$ mice (*SI Appendix*, Fig. S3). As previous studies reported that *Irg1*-deficient mice have increased hepatic lipid accumulation in models of fatty liver disease (30), we investigated whether *Irg1* affects macrophage cholesterol handling and foam cell formation in vitro. *Irg1*$^{-/-}$ BMDMs treated with oxLDL for 48 h showed a marked increase in intracellular lipid content compared to similarly treated WT BMDMs, as assessed by BODIPY staining of neutral lipids (Fig. 3*C*). These data suggest an important role for *Irg1* in restricting macrophage cholesterol accumulation and foam cell formation.

To assess whether the increased accumulation of lipid-laden macrophages in *Irg1*$^{-/-}$ → *Ldlr*$^{-/-}$ plaques was associated with markers of plaque vulnerability, we quantified smooth muscle cell (SMC) abundance via immunostaining of ACTA2 and measured necrotic core area. We observed a trend toward reduced plaque SMC content and a significant increase in the ratio of macrophage-to-SMC in *Irg1*$^{-/-}$ → *Ldlr*$^{-/-}$ plaques (Fig. 3 *D* and *E*), a feature found in inflammatory plaques. However, we observed no difference in necrotic core area in *Irg1*$^{-/-}$ → *Ldlr*$^{-/-}$ mice compared to WT → *Ldlr*$^{-/-}$ mice (Fig. 3*F*).

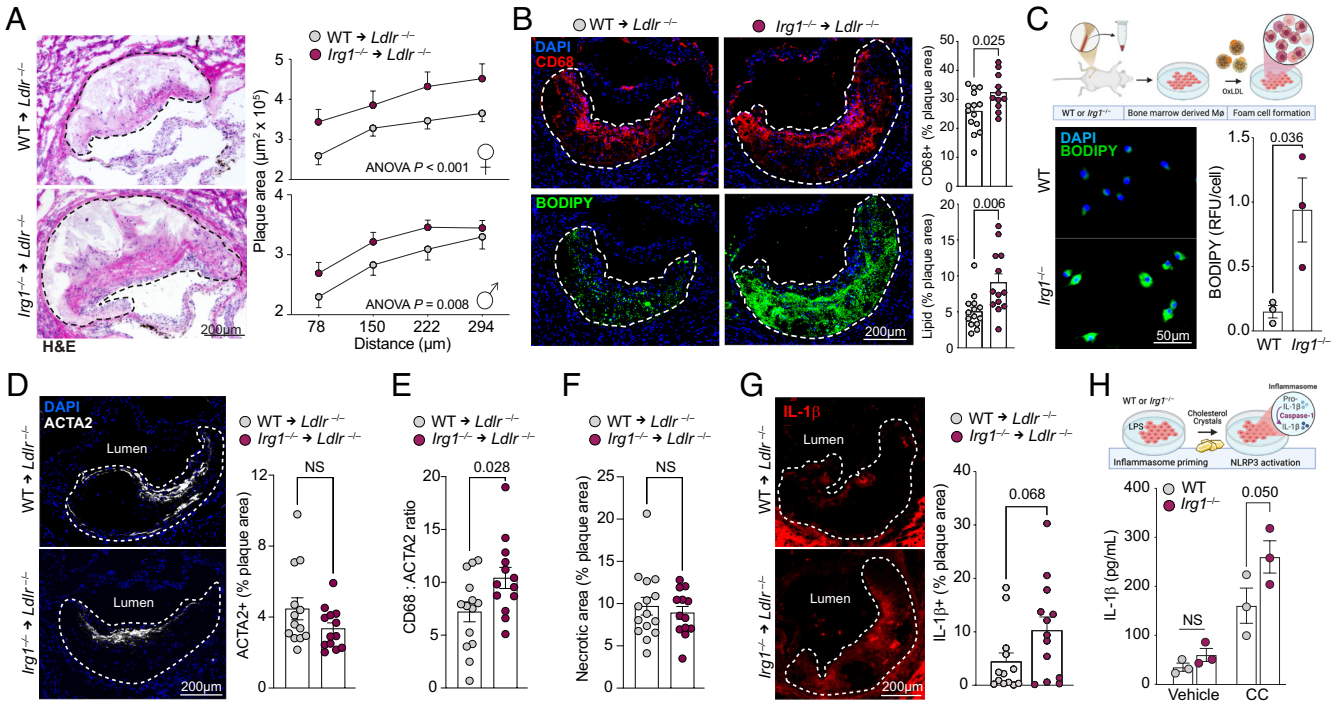

Fig. 3. Myeloid *Irg1* expression protects against atherosclerosis development. (*A* and *B*) Aortic root plaques of male and female *Ldlr*$^{-/-}$ mice reconstituted with bone marrow from WT (WT → *Ldlr*$^{-/-}$) or *Irg1*$^{-/-}$ (*Irg1*$^{-/-}$ → *Ldlr*$^{-/-}$) mice and fed WD (12 wk), showing representative staining and quantification of (*A*) H&E and plaque area through the aortic root, and (*B*) CD68 and BODIPY neutral lipid stain in male mice. (*C*) Neutral lipid accumulation in BMDMs from WT or *Irg1*$^{-/-}$ mice treated with oxLDL (50 μg/mL, 48 h) as assessed by BODIPY staining and quantification of relative fluorescence intensity (RFU). (*D*–*G*) Immunostaining and quantification of (*D*) ACTA2, (*E*) CD68 to ACTA2 ratio, (*F*) necrotic area, and (*G*) IL-1β in aortic root plaques of WT → *Ldlr*$^{-/-}$ or *Irg1*$^{-/-}$ → *Ldlr*$^{-/-}$ male mice. (*H*) Quantification of IL-1β secretion in BMDMs from WT and *Irg1*$^{-/-}$ mice primed with LPS (10 ng/mL, 4 h) and activated with CC (500 μg/mL, 8 h). *P*-values were calculated by (*A*) two-way ANOVA for group differences (genotypes), (*B*–*G*) Student's *t* test, (*H*) two-way ANOVA with Sidak's multiple-comparison test. (*A*, *B*, and *D*–*G*) n = 13 to 14 mice/group/sex. (*C*) n = 3 individual mouse/group.

Notably, we also observed a marked increase in immunostaining for IL-1β in plaques of *Irg1*$^{-/-}$ → *Ldlr*$^{-/-}$ mice compared to WT → *Ldlr*$^{-/-}$ mice (Fig. 3*G*). *Irg1*-deficiency has been reported to increase NLRP3-inflammasome activation and maturation of pro-IL-1β during infection (17), but whether it regulates inflammasome activation in atherosclerosis remains unclear. To test this, we first primed WT and *Irg*$^{-/-}$ BMDMs with LPS, and then exposed them to CC, an atherogenic activator of inflammasome assembly and caspase-1 activation (5, 6). We found that CC-induced IL-1β secretion was potentiated in *Irg*$^{-/-}$ BMDM compared to WT BMDM (Fig. 3*H*), consistent with increased inflammasome activation.

***Irg1* Dampens Proinflammatory Cross-Talk between Macrophages and Neutrophils.** Our cell–cell communication analysis (Fig. 2*K*) indicated important anti-inflammatory cross-talk between *Lyve1*$^{+}$ macrophages and neutrophils that was absent in *Irg1*-deficient mice. Neutrophils contribute to inflammation in the plaque through the production of NETs (7), ROS, and proteases, which are triggered by CC (31, 32). Consistent with a role for *Irg1* and itaconate in restricting neutrophil proatherogenic responses, we measured a significant increase in NET accumulation in plaques of *Irg1*$^{-/-}$ mice compared to WT mice, as assessed by immunostaining for myeloperoxidase (MPO) and citrullinated histone H3 (CitH3, Fig. 4*A*). To test whether this effect was cell autonomous, we isolated neutrophils from the bone marrow of WT and *Irg1*$^{-/-}$ mice, stimulated with PMA (100 nM) or vehicle (DMSO), and quantified NET formation via user-trained deep-learning image analysis in the IncuCyte platform. In PMA-stimulated neutrophils, NETosis was potentiated in absence of *Irg1* (Fig. 4*B*). Further, compared to WT neutrophils, *Irg1*$^{-/-}$ neutrophils elaborated more NET DNA in response to CC (Fig. 4*C*). Notably, NETs can activate surrounding macrophages by priming the NLRP3-inflammasome, leading to increased expression of *pro-IL1b* and inflammasome components (e.g., *Pycard*, *Casp1* and *Nlrp3*). To test whether *Irg1* regulates this neutrophil-macrophage cross talk, we collected NET DNA from neutrophils exposed to CC and applied it on WT and *Irg1*$^{-/-}$ BMDMs (Fig. 4*D*; steps 1 and 2). We observed higher levels of *Il1b* and *Pycard* mRNA in *Irg1*$^{-/-}$ compared to WT BMDM, indicating increased NLRP3 inflammasome priming (Fig. 4*E*), and exposure of NET-primed BMDMs to CC (step 3) resulted in increased IL-1β secretion from *Irg1*$^{-/-}$ BMDM compared to WT (Fig. 4*F*). Collectively, these data highlight the role of Irg1 in tempering the inflammatory cross talk by neutrophils and macrophages that regulates inflammasome priming and activation in atherosclerosis.

IRG1–Itaconate Axis Supplementation Induces Beneficial Plaque Remodeling in Mice. Our data suggest that levels of *Irg1*, and thus itaconate, decrease with plaque progression in mice (Fig. 1*H*), indicating that itaconate supplementation could have therapeutic potential in atherosclerosis. To investigate this, we tested the ability of the cell-permeable itaconate derivative 4-OI to restrict neutrophil NETosis and macrophage NLRP3-inflammasome activation. Treatment with 4-OI decreased CC-induced NET formation in vitro by ~50% (Fig. 5*A*). Furthermore, in LPS-primed BMDMs, 4-OI abrogated inflammasome activation and IL-1β secretion in response to CC or ATP (Fig. 5*B*). Given these beneficial effects, we conducted a 4-wk trial of 4-OI or vehicle administration (intraperitoneal injection, 3x/week) in *Ldlr*$^{-/-}$ mice with advanced, complex atherosclerotic plaques induced by 30-wk WD feeding (Fig. 5*C*). Administration of 4-OI induced favorable changes in plaque morphology, characterized by marked reductions in plaque macrophage content (Fig. 5*D*) and necrotic core area (Fig. 5*E*).

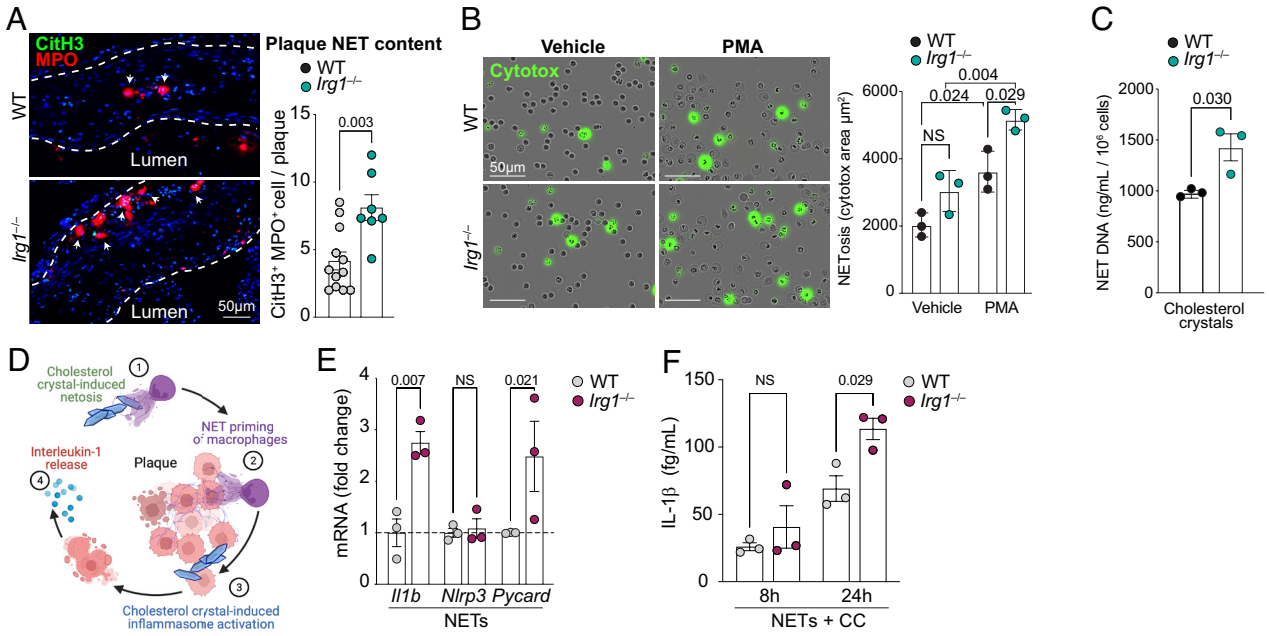

Fig. 4. *Irg1* mitigates proinflammatory cross-talk between macrophages and neutrophils. (*A*) Representative staining and quantification for the extracellular trap markers citrunillated-H3 (CitH3) and myeloperoxidase (MPO) in aortic root plaques from male WT and *Irg1*$^{-/-}$ mice fed WD (12 wk). (*B*) Visualization of NETosis with Cytotox DNA dye and quantification per field of view (FOV, 4 FOV/well in triplicates) in bone marrow-derived neutrophils from WT and *Irg1*$^{-/-}$ mice stimulated with vehicle or PMA (100 nM, 4 h). (*C*) Quantification of NET-DNA extrusion from WT or *Irg1*$^{-/-}$ neutrophils treated with CC (500 μg/mL, 4 h). (*D*) Schematic of proposed pathway showing priming of macrophages by CC-induced NETs, leading to CC-induced inflammasome activation and IL-1β release. (*E*) qRT-PCR quantification of NLRP3-inflammasome priming genes in WT and *Irg1*$^{-/-}$ BMDM treated with NET-DNA from neutrophils exposed to CC. (*F*) Quantification of IL-1β secretion in WT and *Irg1*$^{-/-}$ BMDM primed with CC-induced NET-DNA and then activated with CC (500 μg/mL, 24 h). *P*-value calculated by (*A* and *C*) Student's *t* test; (*B*, *E*, and *F*) two-way ANOVA with Sidak's MCT. (*A*) n = 6 to 12 mice, (*B–F*) n = 3 individual mouse/group.

Moreover, 4-OI reduced the proportion of complex, advanced plaques (Fig. 5*F*; stage V, Stary classification), in the absence of changes in plaque size (Fig. 5*D*), consistent with beneficial plaque remodeling in treated mice. Notably, 4-OI treatment reduced IL-1β immunostaining in plaques (Fig. 5*G*), consistent with our in vitro findings that 4-OI reduces NLRP3-inflammasome activation by CC.

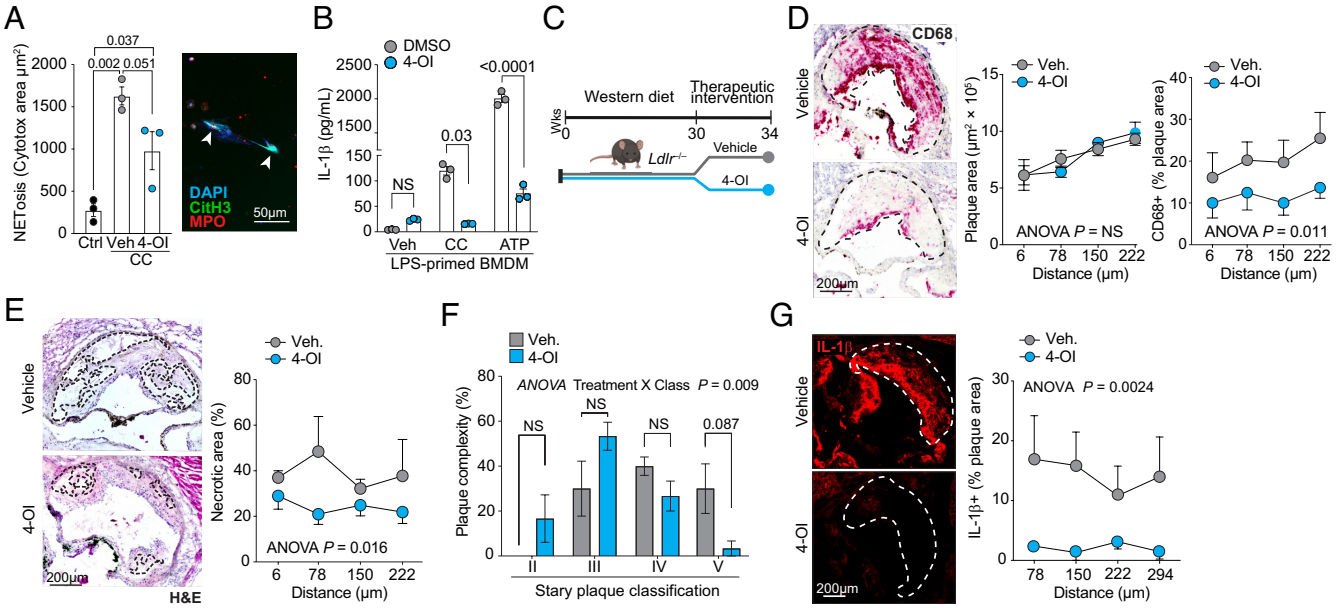

Fig. 5. Itaconate reduces atherogenic inflammation and remodels the atherosclerotic plaque. (*A*) Representative NETosis imaging showing colocalization (arrows) of citrunillated-H3 (CitH3) and DNA (DAPI) around a neutrophil (MPO), and quantification by IncuCyte live cell imaging in bone marrow-derived neutrophils untreated (Ctrl) or pretreated with 4-OI (500 μM, 1 h) and stimulated with CC (500 μg/mL, 4 h). (*B*) IL-1β secretion by LPS-primed BMDM pretreated with vehicle or 4-OI (250 μM, 1 h) and activated with CC (500 μg/mL, 8 h) or ATP (5 mM, 2 h) as a positive control. (*C*) Experimental design of 4-OI therapeutic intervention in *Ldlr*$^{-/-}$ male mice fed WD for 34 wk and injected interperitoneally during the last 4 wk of diet with 4-OI (25 mg/kg) or vehicle (7.5% DMSO). (*D*) Representative CD68 staining and quantification in aortic root plaques of 4-OI or vehicle-treated mice. (*E*) Representative H&E staining and quantification of the necrotic area in aortic root plaques of 4-OI or vehicle-treated mice. (*F*) Histological classification of aortic root plaques according to Stary: II, moderate lesions; III, preatheroma; IV, atheroma; V, fibroatheroma. (*G*) Representative IL-1β immunostaining and quantification in aortic root plaques of 4-OI or vehicle-treated mice. *P*-value calculated by (*A*) one-way ANOVA with Tukey's MCT; (*B*) two-way ANOVA with Sidak's MCT; (*D*, *E*, and *G*) two-way ANOVA with group differences (treatment), (*F*) two-way ANOVA with interaction between Stary classification and treatment.

Therapeutic Use of 4-OI Improves CVD-Related Inflammation in Humans Ex Vivo. To assess the therapeutic potential of 4-OI in humans, we leveraged a validated systems-immunology approach to investigate CVD-related inflammation ex vivo (33). We isolated PBMCs from healthy donors (n = 6) and incubated them with plasma from patients with carotid atherosclerosis (CVD plasma) with or without pretreatment with 4-OI (250 μM; n = 4 for all conditions, Fig. 6*A*). To assess the inflammatory signaling events that occur in response to treatment with CVD plasma, we used phosphocytometry by time-of-flight (phospho-CyTOF) to resolve phosphosignaling at the single-cell level. Using viSNE, we identified 11 major immune cell populations based on canonical marker expression patterns [CD1c$^+$ dendritic cells (DC), CD14$^+$ monocytes, CD16$^+$ monocytes, CD14/16$^+$ monocytes, plasma DCs, B cells, CD4$^+$ and CD8$^+$ T cells, exhausted T cells, natural killer (NK) cells, and basophils] (Fig. 6*B*), and then quantified the phosphorylation of seven intracellular proteins–AKT serine/threonine kinase 1 (AKT), nuclear factor of κ light chain polypeptide gene enhancer in B cells inhibitor-α (IκBα), mitogen-activated protein (MAP) kinase-activated protein kinase 2 (MAPKAPK2), ribosomal protein S6 (pS6), phosphorylated cAMP-response element binding protein (pCREB), and extracellular signal-regulated kinase 1 and 2 (pERK1/2) across immune populations and treatments (Fig. 6 *C* and *D*). Because of the restricted expression of *Irg1* in myeloid cells, we focused our analysis on monocyte populations, where we observed a relative increase in AKT, MAPKAPK2, CREB, ERK1/2 and S6 kinase signaling upon treatment with CVD plasma, which was in turn, attenuated by 4-OI pretreatment (Fig. 6*D*). The significant increase in phospho-signaling following CVD plasma treatment could be visualized by t-statistics, with phosphorylated proteins showing consistent upregulation in all three monocyte subtypes (Fig. 6 *E*, *Top*). 4-OI supplementation reverted this pattern, with significant decreases in pCREB in CD14/16$^+$ and CD14$^+$ monocytes, and pS6 in CD16$^+$ monocytes, and a trending decrease for all phosphoproteins across these cell populations (Fig. 6 *E*, *Bottom*).

To determine how 4-OI affects the transcriptional signature of human immune cells exposed to CVD plasma, we next performed scRNA-seq of treated PBMCs. CVD plasma induced significant increases in abundance of both *CD163*$^+$ and *PLIN2*$^+$ macrophage subpopulations ($P = 3.48 \times 10^{-6}$ and 1.15×10^{-5}, respectively) at the expense of the *CD14*$^+$ monocyte cluster ($P = 3.48 \times 10^{-6}$), evidence of a transition from a naïve to a mature state following stimulation (Fig. 6*F* and *SI Appendix*, Fig. S4*A*). *IRG1* expression was detected across all myeloid cell populations, and was highest in monocytes and macrophages (Fig. 6*F*). While CVD plasma stimulation decreased *IRG1* expression, this was prevented by 4-OI pretreatment, particularly in *CD14*$^+$ monocytes (Fig. 6*G* and *SI Appendix*, Fig. S4*B*). No changes were detected in the abundance of T cell subpopulations, with the exception of double-negative T cells marked by expression of the chemokine gene *CXCL3* (34), that amounted to less than 1% of that group (*SI Appendix*, Fig. S4*C*), indicating that CVD plasma stimulation primarily affects innate immune cell populations. Of those, *CD163*$^+$ and *PLIN2*$^+$ macrophages displayed the highest number of differentially expressed genes (DEG) between the CVD plasma and CVD plasma + 4-OI conditions (Fig. 6*H*). *PLIN2*$^+$ macrophages, which highly express the *PLIN2* gene encoding a protein that coats intracellular lipid droplets, have been implicated with both lipid loading and inflammation within human atherosclerotic plaques (35), whereas *CD163*$^+$ highly express *CD163*, a scavenger receptor associated with downstream anti-inflammatory responses through IL-10 signaling (36). Canonical pathway analyses of genes differentially expressed in these macrophage populations in the presence of 4-OI showed an upregulation of NRF2 and IL-10 signaling, and a downregulation of genes that contribute to neutrophil degranulation (Fig. 6 *H* and *I*). Consistent with this, in silico modeling of cell–cell interactions predicted that the bulk of IL-10 signaling took place through *CD163*$^+$ macrophages, and this was increased by 4-OI pretreatment (Fig. 6*J*). These data show that *IRG1* expression by myeloid cells declines in the CVD environment and that 4-OI supplementation can up-regulate antioxidant and anti-inflammatory transcriptional programs that protect from atherosclerosis.

Discussion

Despite progress in the prevention and treatment of atherosclerosis using cholesterol-lowering medications, a considerable burden of residual CVD risk remains in many patients. Targeting inflammation has shown promise in treating atherosclerotic disease, as demonstrated by the CANTOS trial in which administration of an anti-IL-1β antibody significantly reduced adverse cardiovascular events (37). However, an increased risk of fatal infections has prevented its use as a therapy. Harnessing metabolic pathways to alter inflammatory cell polarization and promote inflammation resolution has gained recent attention as a new therapeutic approach in chronic inflammatory diseases. Here, we establish a role for *Irg1* and its metabolic product itaconate as proresolving mediators of inflammation in atherosclerotic plaques that can be exploited to treat CVD.

The expression profile of *IRG1* across cell populations in human chronic inflammatory pathologies remains largely unexplored. Using patient-matched scRNA-seq data coupled with immunostaining analyses, we compared IRG1 expression in pathological FAs in coronary arteries to regions of normal AIT. Our findings revealed that IRG1 is enriched in atherosclerotic tissue and is predominantly expressed in monocytes and macrophages. We observed a similar distribution of IRG1 expression in carotid plaque specimens obtained from human subjects undergoing carotid endarterectomy. Using timed diet-induced atherosclerosis studies in mice, we show that while expression of *Irg1* is high in monocytes and neutrophils that invade early atherosclerosis lesions, its expression declines in more advanced plaques. While the mechanisms underlying the decrease in IRG1 remain unidentified, our data suggest that this anti-inflammatory axis wanes with disease progression. The significance of this is underscored by our findings that global or hematopoietic *Irg1* deficiency increases atherosclerotic burden and indices of plaque inflammation, including heightened macrophage content, lipid burden, and IL-1β. Accordingly, scRNA-seq analysis showed enrichment in lipid-loaded macrophages, proinflammatory rewiring of resident-like macrophages, and decreased predicted anti-inflammatory cell-to-cell communication in plaques of mice deficient in *Irg1*. Our data are consistent with a recent report showing that total IRG1 expression in coronary plaques is negatively correlated with clinical occlusion (38), and that myeloid *Irg1* deletion in mice increases plaque size and markers of inflammation (38). Together, these findings highlight the importance of IRG1 in repressing atherosclerotic inflammation protecting from plaque progression.

Our studies also unveiled a role for IRG1 in restricting detrimental neutrophil-macrophage cross talk in the plaque, fueled by CC, that primes and activates the NLRP3-inflammasome and triggers the secretion of IL-1β. Expression of *Irg1* and itaconate were increased in macrophages and neutrophils treated with aggregated and oxidized forms of LDL that accumulate in the artery wall and incite atherosclerotic inflammation. While the underlying mechanisms remain to be investigated, oxLDL can trigger toll-like receptor and

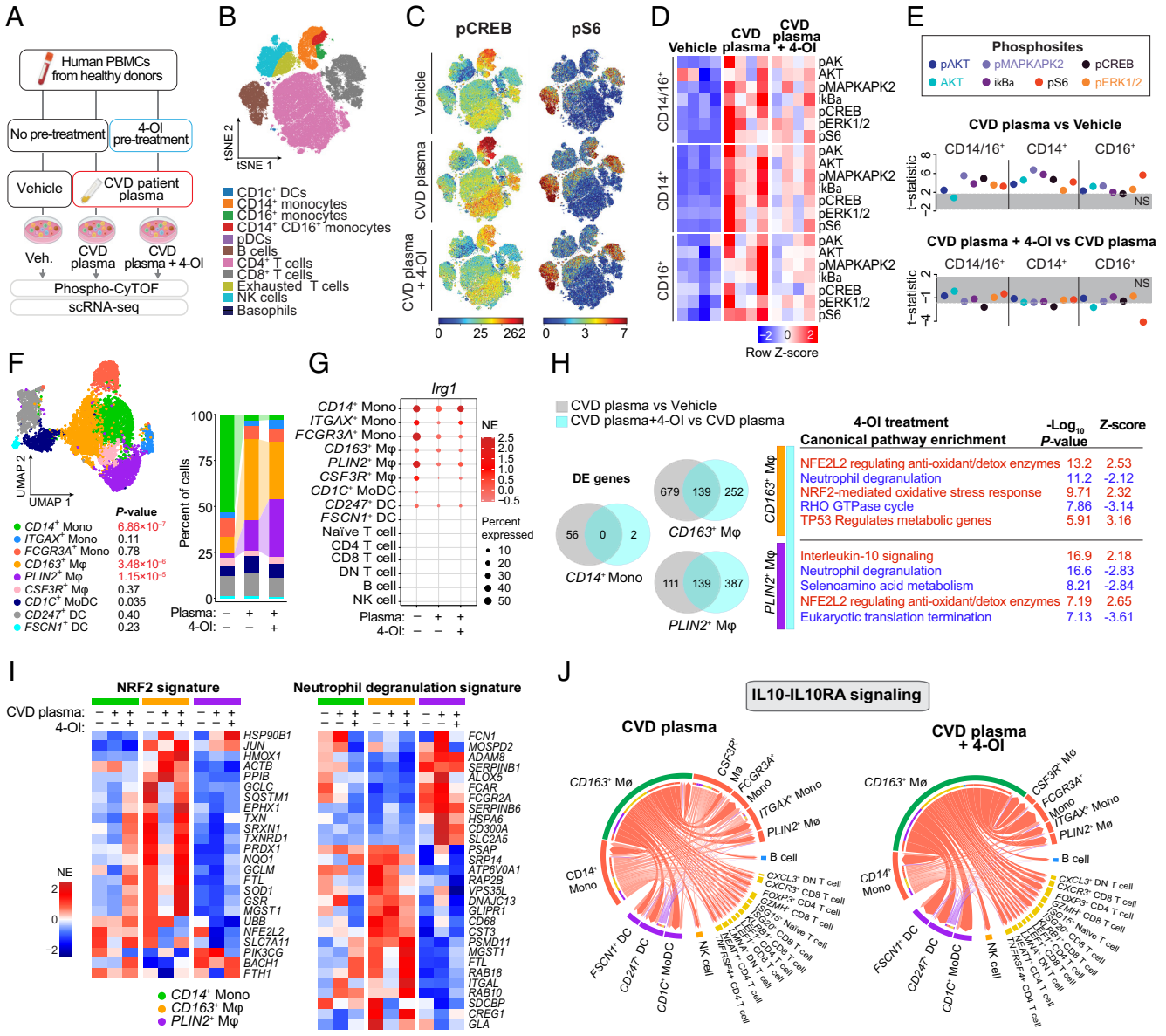

Fig. 6. Itaconate derivative reduces CVD plasma-associated inflammation. (*A*) Schematic of experimental design. Human PBMCs isolated from healthy donors were treated with vehicle (Veh) or plasma from patients with CVD (plasma, n = 4), with or without pretreatment with 4-OI (250 μM; CVD plasma + 4-OI), and subjected to phospho-cytometry by time-of-flight (phospho-CyTOF) and scRNA-seq. (*B*) Representative viSNE plot of PBMCs showing major immune cell subsets based on canonical expression marker. (*C* and *D*) Representative viSNE visualization of pCREB and pS6 levels in major immune cell subsets (*C*), and heatmap of phosphorylation levels in $CD14^+$, $CD16^+$, and $CD14/16^+$ monocyte populations (*D*) quantified by phospho-CyTOF. (*E*) t-Statistics visualization of monocyte-specific phosphorylation, with positive values outside the gray box indicating significant upregulation and negative value downregulation comparing CVD plasma to vehicle (*Top*), or CVD plasma + 4-OI treatment vs. CVD plasma (*Bottom*). (*F*) UMAP visualization of myeloid PBMCs analyzed by scRNA-seq (*Left*) and frequency of cell populations identified, stratified by treatment group. (*G*) Average *IRG1* expression by cell type. NE = normalized expression. (*H*) Venn diagram depicting shared DEG between vehicle vs. CVD plasma, and CVD plasma + 4-OI vs. CVD plasma in $CD163^+$ Mø and $PLIN2^+$ Mø (*Left*) with canonical pathway enrichment analyses of DEGs (*Right*). (*I*) Normalized gene expression matrix showing differential transcriptional signature for NRF2 and neutrophil degranulation pathways between treatment groups in indicated myeloid populations. (*J*) Chord diagram of predicted IL10-IL10RA signaling between PBMC populations treated with CVD plasma (*Left*) or CVD plasma + 4-OI (*Right*). (*E*) t-Statistics significance threshold set at ±1.638 (df: 3, $P < 0.1$); (*F*) *P*-value by one-way ANOVA. n = 4 independent plasma samples per condition.

type I IFN signaling known to drive *Irg1* expression (11, 39, 40). We show that expression of *Irg1* in neutrophils restricts cholesterol crystal-induced NETosis and the elaboration of NETs that prime the NLRP3-inflammasome in surrounding macrophages. Previous studies have shown that itaconate limits ROS generation and glycolysis, both of which are critical for NETosis (41, 42). Further, expression of *Irg1* in macrophages reduces activation of the NLRP3-inflammasome by CC and secretion of IL-1β. These data establish an *Irg1*-centric cross talk between neutrophils and macrophages that curbs the release of IL-1β, a potent proinflammatory cytokine that fuels both local and systemic proatherosclerotic inflammation (5, 6, 23). Notably, we also observed an increase in plaque lipid accumulation associated with *Irg1* deficiency, and showed in vitro that foam cell formation induced by exposure of macrophages to oxLDL was augmented with *Irg1* deficiency. We have previously shown that oxLDL-induced foam cell formation leads to the intracellular nucleation of CC that can destabilize lysosomes and trigger the NLRP3-inflammasome (5), and thus, the increase in foam cell formation in $Irg1^{-/-}$ mice may establish a feed-forward loop that enhances NLRP3-inflammasome activation. In addition to cleaving pro-IL-1β into its mature form, this process also induces pyroptosis, a necrotic form of regulated cell death that

would result in the release of intracellular CC, along with mature IL-1β, into the plaque microenvironment. The relevance of this lipid-induced feed-forward cycle, where inflammation begets more inflammation, is highlighted by our findings of increases in lipid burden, macrophage accumulation, NETosis, and IL-1β in plaques of *Irg1*$^{-/-}$ mice.

In support of the IRG1–itaconate axis having a protective role against lipid-induced metabolic inflammation, itaconate has been reported to protect against nonalcoholic fatty liver disease in mice by reducing hepatic lipid accumulation through β-oxidation (30). In our transcriptomic pathway analysis of resident-like macrophages, we showed that *Irg1*-deficiency was associated with a decrease in OXPHOS, generally indicative of a metabolic shift from fatty acid oxidation to glycolysis in activated macrophages (43), and with an upregulation of PPAR signaling, suggestive of an increased intracellular fatty acid load (44). Interestingly, a number of lipids in the plaque derived from fatty acids (45), modified lipoproteins (e.g., oxLDL) (5), and CC (6), can prime and/or activate the NLRP3 inflammasome leading to IL-1β secretion in macrophages. In our model, deletion of *Irg1* led to concomitant lipid accumulation and increased IL-1β abundance in the plaque, suggesting that *Irg1* controls metabolic changes in macrophages that dampen lipid-mediated inflammation and IL-1β release in atherosclerosis.

Our human and murine data support that reduced metabolic flux through IRG1 has deleterious effects on atherosclerosis progression, and thus supplementing this axis holds therapeutic potential. Indeed, therapeutic administration of the itaconate-derivative 4-OI in mice with advanced atherosclerosis induced beneficial plaque remodeling characterized by reductions in plaque complexity, macrophage content, and IL-1β expression, despite ongoing WD feeding. Our findings complement recent studies showing that 4-OI can prevent atherosclerosis progression in mice when administered concurrently with WD feeding for 10 wk, in part through an NRF2-dependent mechanism (38). Furthermore, using a systems biology approach validated for CVD drug-repurposing studies (33) we resolve, with single-cell granularity, the effects of 4-OI on human immune cell populations in the context of CVD inflammation. Treatment of human PBMCs with 4-OI attenuated the rapid proinflammatory signaling cascade induced by CVD patient plasma, as assessed by phospho-CyTOF and scRNA-seq. This modeling of the impact of systemic atherosclerotic inflammation on circulating immune cell populations showed that IRG1 expression declines in monocyte and macrophage populations exposed to a CVD environment, and that 4-OI supplementation both modulates macrophage inflammatory commitment and restores antioxidant and anti-inflammatory pathways. Specifically, we found that 4-OI pretreatment reversed the rapid phosphorylation of AKT, MAPKAPK2, CREB, ERK1/2, and S6 kinases in CD14^{+} and CD16^{+} monocyte populations induced by CVD plasma. Further, 4-OI significantly inhibited phosphorylation of CREB, a transcription factor that is central to the transcriptional reprogramming triggered by CVD plasma in monocytes (33). Parallel scRNA-seq analysis showed that 4-OI modulates monocyte identity commitment in response to CVD plasma, and stimulates anti-inflammatory and NRF2-dependent antioxidant pathways at the transcriptional level in *CD163*$^{+}$ and *PLIN2*$^{+}$ macrophages. Notably, 4-OI treatment positively impacts predicted *CD163*$^{+}$-mediated cell–cell signaling via IL-10, an anti-inflammatory cytokine with numerous atheroprotective functions (46).

Taken together, our studies in humans and mice identify important roles for the IRG1–itaconate axis in protecting from atherosclerosis, and show that these protective functions diminish in the chronic inflammatory milieu of the plaque as disease progresses. We establish that augmenting this axis with 4-OI holds therapeutic promise as evidenced by its ability to remodel complex atherosclerotic plaques in mice, and rewire inflammation in a model of human systemic CVD inflammation.

Material and Methods

Expanded methods are found in *SI Appendix*.

Human Coronary Samples. Two patients with end-stage heart failure undergoing heart transplantation were enrolled in a clinical study approved by the Institutional Review Board (IRB) (IRB no. 21-00429). Patient characteristics are detailed in *SI Appendix*, Table S1. Inclusion criteria were patients over 18 y old undergoing heart transplantation at NYU Langone Health for either ischemic or nonischemic heart failure. Exclusion criteria were active infection, autoimmune diseases, peripheral arterial occlusive disease with rest pain, and renal dialysis. Sections of the same coronary arteries were stained with hematoxylin and eosin (H&E) and classified as AIT and FA according to established criteria, as described (47, 48).

scRNA-seq of Human Coronary Cells. Single-cell suspensions were prepared from the left anterior descending and right coronary artery immediately after heart removal. Briefly, plaques were washed extensively, digested, and sequentially filtered before removal of dead cells and automated counting. scRNA-seq libraries were prepared using the Chromium Next GEM Single Cell 3′ GEM, Library & Gel Bead Kit v3.1, Chip G Single Cell Kit and Dual Index Kit TT Set A (10× Genomics; PN-1000268, PN-1000127, PN-100215). DNA library quality was measured by Qubit dsDNA, and sequenced on an Illumina NovaSeq X+ sequencer as described (49).

Immunofluorescence Staining of Human Coronary Artery and Carotid Endarterectomy. Eight patients undergoing carotid endarterectomy (CEA) were enrolled in a clinical study approved by the IRB of NYU Langone Health (IRB no. 21-00429) and the Icahn School of Medicine at Mount Sinai (IRB no. 11-01427). Patient characteristics and inclusion and exclusion criteria are described elsewhere (47, 49). Paraffin-embedded tissues were processed as described (47). Samples were costained for IRG1 and CD68 (*SI Appendix*, Table S2) and counterstained for nuclei (DAPI, Invitrogen D1306). Autofluorescence was quenched with TrueBlack Lipofuscin Autofluorescence Quencher (Biotium, Cat. #23007). Images were acquired on a Phenoimage HT (Akoya Biosciences), and manually outlined before spectral unmixing and quantitative analysis, as described (47).

Mouse Studies. All experimental procedures were approved by the NYU Grossman School of Medicine's Institutional Animal Care and Use Committee and conducted in accordance with the US Department of Agriculture Animal Welfare Act and the US Public Health Service Policy on Humane Care and Use of Laboratory Animals. Atherosclerosis was induced in male or female *Ldlr*$^{-/-}$ mice (Jackson Lab: #002077), by WD (21% [wt/wt] fat, 40% fat kcal, 0.3% cholesterol; Dyets 101977GI) feeding for 12 to 16 wk. Atherosclerosis was induced in 8-wk-old *Irg1*$^{-/-}$or control C57BL/6NJ (Jackson Lab: #029340, #005304) male mice by delivery of D377Y-mPCSK9 by AAV (Penn Vector core) and WD feeding for 12 to 16 wk as described (25). To evaluate the effects of 4-OI on advanced atherosclerotic plaques, 8-wk-old *Ldlr*$^{-/-}$ male mice were fed WD for 30 wk to induce atherosclerosis and treated 4-OI (25 mg/kg *i.p.* in corn oil; MedChem Express, HY-112675) or vehicle (7.5% DMSO in corn oil) 3x/week for 4 wk (n = 5 mice/group). For transplant studies, bone marrow cells from male or female *Irg1*$^{-/-}$ or C57BL/6NJ were retro-orbitally transferred into lethally irradiated (2 × 4.5 Gy, administered 3 h apart) male or female *Ldlr*$^{-/-}$ mice (n = 3 mice/genotype/sex donor, n = 13 to 15 mice/group/sex recipient), and mice were kept on antibiotic-containing water for 5 wk. After one additional week of recovery, mice were placed on WD for 12 wk. Bone marrow chimerism was assessed by PCR (primers used are listed in *SI Appendix*, Table S3).

Atherosclerosis Analyses. Mice with cholesterol <525 mg/dL were excluded from the study. Heart, aorta, and blood were collected and processed as described (25). Morphometric analysis of plaque burden, necrotic area, and plaque complexity was performed using ImageJ software (https://fiji.sc/) as described (25). To assess plaque composition, immunohistochemical and histochemical staining was performed to evaluate neutral lipid content (BODIPY), NETosis (Citrullinated H3, MPO), IRG1, CD68, Ly6G, and ACTA2 as described (25). Aortic arches were digested, filtered through a 70-μm strainer, stained for viability and CD45 expression, and hashtagged. Live CD45^{+} cells were purified by fluorescence-activated cell sorting using

a BD FACSAria II instrument equipped with a 100 μm nozzle, and specimens were pooled by the experimental group (n = 5/group), and scRNA-seq performed as described above for human coronary plaques and in *SI Appendix* (25).

scRNA-seq Analysis. scRNA sequencing data alignment, preprocessing, filtering, normalization, dimensionality reduction, and visualization followed protocols established in previous human (49) and mouse (25) studies. Briefly, in human coronary plaque, Louvain clustering revealed 23 distinct cell populations. Subsequent subclustering of myeloid cells identified nine distinct groups, with a total of 3,556 myeloid cells sequenced and annotated. For CD45+ cells from aortic arch plaques in *Ldlr*$^{-/-}$ mice, 21 distinct populations were identified using Louvain clustering. Subclustering on monocytes, macrophages, DCs, and neutrophils (myeloid cells) identified 8,669 myeloid cells. For immune cells from aortic arch plaques of WT and *Irg1*$^{-/-}$ mice, 20 distinct populations were identified by Louvain clustering, with 6,022 cells sequenced. For human PBMCs, initial clustering with the Louvain algorithm identified 20 distinct major populations, with a total of 41,407 cells sequenced. Further subclustering identified 23 distinct subpopulations of myeloid cells and T cells. Immune cells within the atherosclerotic plaque were annotated based on expression of canonical gene markers identified for human (49) and mouse (50) atherosclerosis. Human PBMCs were annotated using established gene markers (33). DEG between cell types were identified using the presto package (v1.0.0) and pathway enrichment analysis was performed using Ingenuity Pathway Analysis software (Qiagen). Cell–cell communication was examined using the CellChat package (v1.6.1) for the entire dataset (29).

Macrophage Atherogenic Ligand Stimulation. Mouse BMDMs were prepared as described (25) and treated with agLDL (50 μg/mL), oxLDL (50 μg/mL; Thermo Fisher L34357) or vehicle for 8 h, or primed with NET-DNA (500 ng/mL, 4 h). To assess the effect of 4-OI on NLRP3-activation, WT BMDMs were primed with LPS (10 ng/mL, 3 h), treated with 4-OI (250 μM) or vehicle for 2 h, and then activated with CC (500 μg/mL, 8 h) or ATP (5 mM, 2 h). Supernatant was collected and IL-1β was measured using BD CBA Mouse IL-1β Enhanced Sensitivity Flex Set (BD, 562278). To induce foam cell formation, BMDMs were treated with oxLDL (50 μg/mL, 48 h), stained with BODIPY, and intracellular neutral lipid was quantified from eight fields of view in triplicate and normalized to cell number. All experiments performed with n = 3 mice/group.

NET Isolation and NETosis Quantification. Mouse neutrophils were isolated from bone marrow of WT and *Irg1*$^{-/-}$ mice using the Neutrophil Isolation Kit (Mitenyi Biotec, 130-097-658). NETosis was assessed using the Incucyte Live-Cell Analysis System (Sartorius) in neutrophils treated with PMA (100 nM), CC (500 μg/mL), or vehicle, and stained with Cytotox Green reagent DNA dye (250 nM, Sartorius). To assess the effect of 4-OI, neutrophils were pretreated with 4-OI (250 μM) for 1 h prior to stimulation. NET-DNA extrusion was measured from neutrophils treated with CC (500 μg/mL, 4 h) as described (7). To detect NETosis in situ, plaques were stained for Histone H3 citrulline R2+R8+R17, MPO, and counterstained with DAPI (*SI Appendix*, Table S2).

Targeted Metabolomics. Targeted metabolomics was performed on BMDMs treated with agLDL (50 μg/mL), oxLDL (50 μg/mL), or vehicle for 24 h by the NYU Metabolomics Core Resource Laboratory, as described (51). Briefly, metabolites were extracted using 80% methanol and a metabolomics amino acid mix standard (Cambridge Isotope Laboratories Inc.), homogenized, centrifuged, dried by speedvac (Thermo Fisher Scientific), and reconstituted in Optima LC/MS grade water (Thermo Fisher Scientific). Samples were sonicated and subjected to LC/MS analysis.

RNA Isolation and Qpcr. Total RNA was isolated, reverse transcribed, and quantitative PCR performed as described (5). Fold change in mRNA expression was calculated using the comparative cycle method ($2^{-\Delta\Delta Ct}$) normalized to housekeeping genes. Primers used are listed in *SI Appendix*, Table S3.

PBMC Stimulation. PBMCs were isolated from whole blood of six healthy donors (patient characteristics are detailed in *SI Appendix*, Table S4) from the New York Blood Center, within 2 h of receipt, as described (49) and stored in liquid N_2 until experiment date. To isolate CVD plasma, fasting peripheral venous blood was preoperatively collected from 4 CVD patients undergoing CEA and enrolled in an IRB-approved clinical study (NYU Langone Health–IRB no. 21-00429 and the Icahn School of Medicine at Mount Sinai–IRB no. 11-01427), as described in ref. 49. Patient characteristics are detailed in *SI Appendix*, Table S5. PBMCs (RPMI, 1% FBS, 1% P/S) were pretreated with 4-OI (250 μM, 1 h), and stimulated with CVD plasma from 4 CVD patients at a final concentration of 20% as described (33) for 15 min for phospho-CyTOF analysis, or for 4 h for scRNA-seq.

Phospho-CyTOF Analysis. PBMCs were labeled with Rh103 viability marker, fixed with formaldehyde, barcoded using the Cell-ID 20-Plex Pd Barcoding Kit (Fluidigm) and labeled with surface antibodies to identify immune subsets, followed by methanol permeabilization and staining with intracellular phosphoprotein antibodies (*SI Appendix*, Table S6), as described (33). Samples were stored in formaldehyde with an iridium intercalator until acquisition using a CyTOF2 Helios mass cytometer (Standard BioTools–FKA Fluidigm). Data normalization and sample processing were performed using Helios software, with barcodes deconvoluted and doublets filtered as described in ref. 49.

Statistics. Statistical significance between two groups of independent biological replicates was evaluated with Student's *t* test; or visually represented using t-statistics. One-way ANOVA was performed when comparing three groups or more for univariate comparisons. Tukey's post hoc multiple comparison test (MCT) was used to compare all groups if the ANOVA revealed significant group differences. Two-way ANOVA was used when comparing two groups or more for bivariate analyses or to assess interaction between two variables, and Sidak's post hoc MCT was used for comparisons between groups selected a priori. Statistical analyses were performed using GraphPad Prism software or R studio. Threshold for statistical significance was $P \leq 0.05$. All quantitative data are presented as mean ± SEM.

Data, Materials, and Software Availability. Sequencing data have been deposited in GEO (GSE252243) (52). All other data are included in the manuscript and/or *SI Appendix*.

ACKNOWLEDGMENTS. Targeted metabolomics was performed at the Metabolomics Core Resource Laboratory, sequencing was performed at Genome Technology Center, and Multispectral imaging was performed at the Experimental Pathology Research Laboratory at the New York University Grossman School of Medicine. This work was supported by grants from the Canadian Institutes of Health Research (MFE-176524 to Y.C.), Chan Zuckerberg Institute (NFL-2020-218415 to C.G.), NIH (F30HL167568 to F.K.B., T32GM136542 to K.M.W. and RVI, R01HL153712 and R01HL165258 to C.G., P01HL146367 to A.M.S., and R35HL135799 to K.J.M., R01HL084312 to E.A.F. and K.J.M., and P01HL131481 to A.M.S., E.A.F., and K.J.M.), and the American Heart Association (19CDA34630066, 23SCEFIA1153739 to C.v.S., 23POST1029885 to M. Gourvest, 20SFRN35210252 to D.D., E.A.F., and C.G., and 915560 to A.A.C.N.).

Author affiliations: [a]Cardiovascular Research Center, New York University Grossman School of Medicine, New York, NY 10016; [b]Department of Anesthesiology and Intensive Care, School of Medicine and Health, Technical University of Munich, Munich 81675, Germany; [c]Division of Endocrinology, Diabetes and Metabolism, New York University Langone Health, New York, NY 10016; [d]Department of Cell Biology, New York University Grossman School of Medicine, New York, NY 10016; and [e]Department of Pathology, New York University Grossman School of Medicine, New York, NY 10016

Author contributions: Y.C., F.K.B., C.G., and K.J.M. designed research; Y.C., F.K.B., L.A., P.S., M. Gourvest, D.D., T.Z., K.M.W., R.V.I., P.M.S., S.D.D., B.F.S., and C.v.S. performed research; A.M.S. contributed new reagents/analytic tools; Y.C., F.K.B., J.G.B.D., A.A.C.N., L.A., P.S., M. Gourvest, D.D., M. Gildea, R.K., T.Z., K.M.W., R.V.I., P.M.S., E.A.F., C.v.S., and C.G. analyzed data; and Y.C., F.K.B., and K.J.M. wrote the paper.

1. P. Libby, Inflammation during the life cycle of the atherosclerotic plaque. *Cardiovasc. Res.* **117**, 2525–2536 (2021).
2. O. Soehnlein, P. Libby, Targeting inflammation in atherosclerosis–From experimental insights to the clinic. *Nat. Rev. Drug Discov.* **20**, 589–610 (2021).
3. K. J. Moore *et al.*, Macrophage trafficking, inflammatory resolution, and genomics in atherosclerosis JACC macrophage in CVD series (part 2). *J. Am. Coll. Cardiol.* **72**, 2181–2197 (2018).
4. O. Soehnlein, Multiple roles for neutrophils in atherosclerosis. *Circ. Res.* **110**, 875–888 (2012).
5. F. J. Sheedy *et al.*, CD36 coordinates NLRP3 inflammasome activation by facilitating intracellular nucleation of soluble ligands into particulate ligands in sterile inflammation. *Nat. Immunol.* **14**, 812–820 (2013).
6. P. Duewell *et al.*, NLRP3 inflammasomes are required for atherogenesis and activated by cholesterol crystals. *Nature* **464**, 1357–1361 (2010).
7. A. Warnatsch, M. Ioannou, Q. Wang, V. Papayannopoulos, Neutrophil extracellular traps license macrophages for cytokine production in atherosclerosis. *Science* **349**, 316–320 (2015).

8. A. Michelucci *et al.*, Immune-responsive gene 1 protein links metabolism to immunity by catalyzing itaconic acid production. *Proc. Natl. Acad. Sci. U.S.A.* **110**, 7820–7825 (2013).
9. L. A. J. O'Neill, M. N. Artyomov, Itaconate: The poster child of metabolic reprogramming in macrophage function. *Nat. Rev. Immunol.* **19**, 273–281 (2019).
10. F. Chen *et al.*, Citraconate inhibits ACOD1 (IRG1) catalysis, reduces interferon responses and oxidative stress, and modulates inflammation and cell metabolism. *Nat. Metab.* **4**, 534–546 (2022).
11. E. L. Mills *et al.*, Itaconate is an anti-inflammatory metabolite that activates Nrf2 via alkylation of KEAP1. *Nature* **556**, 113–117 (2018).
12. A. Hooftman *et al.*, The immunomodulatory metabolite itaconate modifies NLRP3 and inhibits inflammasome activation. *Cell Metab.* **32**, 468–478.e7 (2020).
13. M. Bambouskova *et al.*, Itaconate confers tolerance to late NLRP3 inflammasome activation. *Cell Rep.* **34**, 108756 (2021).
14. S.-T. Liao *et al.*, 4-Octyl itaconate inhibits aerobic glycolysis by targeting GAPDH to exert anti-inflammatory effects. *Nat. Commun.* **10**, 5091 (2019).
15. V. Lampropoulou *et al.*, Itaconate links inhibition of succinate dehydrogenase with macrophage metabolic remodeling and regulation of inflammation. *Cell Metab.* **24**, 158–166 (2016).
16. J. Dominguez-Andres *et al.*, The itaconate pathway is a central regulatory node linking innate immune tolerance and trained immunity. *Cell Metab.* **29**, 211–220.e5 (2019).
17. C. G. Peace, L. A. O'Neill, The role of itaconate in host defense and inflammation. *J. Clin. Invest.* **132**, e148548 (2022).
18. S. Nair *et al.*, Irg1 expression in myeloid cells prevents immunopathology during M. tuberculosis infection. *J. Exp. Med.* **215**, 1035–1045 (2018).
19. M. Bambouskova *et al.*, Electrophilic properties of itaconate and derivatives regulate the IκBζ–ATF3 inflammatory axis. *Nature* **556**, 501–504 (2018).
20. J. D. Bailey *et al.*, Nitric oxide modulates metabolic remodeling in inflammatory macrophages through TCA cycle regulation and itaconate accumulation. *Cell Rep.* **28**, 218–230.e7 (2019).
21. N. L. Fischer, S. Shin, I. E. Brodsky, Jack-of-all-trades: Itaconate tolerizes NLRP3 inflammasome activation. *Cell Rep.* **34**, 108855 (2021).
22. G. Cadby *et al.*, Comprehensive genetic analysis of the human lipidome identifies loci associated with lipid homeostasis with links to coronary artery disease. *Nat. Commun.* **13**, 3124 (2022).
23. P. Libby, Interleukin-1 beta as a target for atherosclerosis therapy: Biological basis of CANTOS and beyond. *J. Am. Coll. Cardiol.* **70**, 2278–2289 (2017).
24. M. Back, A. Yurdagul Jr., I. Tabas, K. Oorni, P. T. Kovanen, Inflammation and its resolution in atherosclerosis: Mediators and therapeutic opportunities. *Nat. Rev. Cardiol.* **16**, 389–406 (2019).
25. M. Schlegel *et al.*, Silencing myeloid netrin-1 induces inflammation resolution and plaque regression. *Circ. Res.* **129**, 530–546 (2021).
26. M. Sharma *et al.*, Regulatory T cells license macrophage pro-resolving functions during atherosclerosis regression. *Circ. Res.* **127**, 335–353 (2020).
27. A. Zernecke *et al.*, Integrated single-cell analysis based classification of vascular mononuclear phagocytes in mouse and human atherosclerosis. *Cardiovasc. Res.* **119**, 1676–1689 (2023), 10.1093/cvr/cvac161.
28. M. T. Patterson *et al.*, Trem2 promotes foamy macrophage lipid uptake and survival in atherosclerosis. *Nat. Cardiovasc. Res.* **2**, 1015–1031 (2023).
29. S. Jin *et al.*, Inference and analysis of cell-cell communication using CellChat. *Nat. Commun.* **12**, 1088 (2021).
30. J. M. Weiss *et al.*, Itaconic acid underpins hepatocyte lipid metabolism in non-alcoholic fatty liver disease in male mice. *Nat. Metab.* **5**, 981–995 (2023).
31. T. Josefs *et al.*, Neutrophil extracellular traps promote macrophage inflammation and impair atherosclerosis resolution in diabetic mice. *JCI Insight* **5**, e134796 (2020).
32. M. Westerterp *et al.*, Cholesterol efflux pathways suppress inflammasome activation, NETosis, and atherogenesis. *Circulation* **138**, 898–912 (2018).
33. L. Amadori *et al.*, Systems immunology-based drug repurposing framework to target inflammation in atherosclerosis. *Nat. Cardiovasc. Res.* **2**, 550–571 (2023).
34. J. C. Crispin, G. C. Tsokos, Human TCR-alpha beta+ CD4- CD8- T cells can derive from CD8+ T cells and display an inflammatory effector phenotype. *J. Immunol.* **183**, 4675–4681 (2009).
35. L. Dib *et al.*, Lipid-associated macrophages transition to an inflammatory state in human atherosclerosis, increasing the risk of cerebrovascular complications. *Nat. Cardiovasc. Res.* **2**, 656–672 (2023).
36. P. Philippidis *et al.*, Hemoglobin scavenger receptor CD163 mediates interleukin-10 release and heme oxygenase-1 synthesis: Antiinflammatory monocyte-macrophage responses in vitro, in resolving skin blisters in vivo, and after cardiopulmonary bypass surgery. *Circ. Res.* **94**, 119–126 (2004).
37. P. M. Ridker *et al.*, Antiinflammatory therapy with canakinumab for atherosclerotic disease. *N. Engl. J. Med.* **377**, 1119–1131 (2017).
38. J. Song *et al.*, Itaconate suppresses atherosclerosis by activating a Nrf2-dependent anti-inflammatory response in macrophages in mice. *J. Clin. Invest.* **134**, e173034 (2023), 10.1172/JCI173034.
39. C. R. Stewart *et al.*, CD36 ligands promote sterile inflammation through assembly of a Toll-like receptor 4 and 6 heterodimer. *Nat. Immunol.* **11**, 155–161 (2010).
40. H. J. Chen, S. W. Tas, M. P. J. de Winther, Type-I interferons in atherosclerosis. *J. Exp. Med.* **217**, e20190459 (2020).
41. O. Rodriguez-Espinosa, O. Rojas-Espinosa, M. M. Moreno-Altamirano, E. O. Lopez-Villegas, F. J. Sanchez-Garcia, Metabolic requirements for neutrophil extracellular traps formation. *Immunology* **145**, 213–224 (2015).
42. T. A. Fuchs *et al.*, Novel cell death program leads to neutrophil extracellular traps. *J. Cell Biol.* **176**, 231–241 (2007).
43. J. Van den Bossche, L. A. O'Neill, D. Menon, Macrophage Immunometabolism: Where are we (going)? *Trends Immunol.* **38**, 395–406 (2017).
44. G. Ye *et al.*, PPARalpha and PPARgamma activation attenuates total free fatty acid and triglyceride accumulation in macrophages via the inhibition of Fatp1 expression. *Cell Death Dis.* **10**, 39 (2019).
45. H. Wen *et al.*, Fatty acid-induced NLRP3-ASC inflammasome activation interferes with insulin signaling. *Nat. Immunol.* **12**, 408–415 (2011).
46. X. Han, W. A. Boisvert, Interleukin-10 protects against atherosclerosis by modulating multiple atherogenic macrophage function. *Thromb. Haemost.* **113**, 505–512 (2015).
47. N. Eberhardt *et al.*, SARS-CoV-2 infection triggers pro-atherogenic inflammatory responses in human coronary vessels. *Nat. Cardiovasc. Res.* **2**, 899–916 (2023).
48. F. Otsuka *et al.*, Natural progression of atherosclerosis from pathologic intimal thickening to late fibroatheroma in human coronary arteries: A pathology study. *Atherosclerosis* **241**, 772–782 (2015).
49. D. M. Fernandez *et al.*, Single-cell immune landscape of human atherosclerotic plaques. *Nat. Med.* **25**, 1576–1588 (2019).
50. H. Winkels *et al.*, Atlas of the immune cell repertoire in mouse atherosclerosis defined by single-cell RNA-sequencing and mass cytometry. *Circ. Res.* **122**, 1675–1688 (2018).
51. D. R. Jones, Z. Wu, D. Chauhan, K. C. Anderson, J. Peng, A nano ultra-performance liquid chromatography-high resolution mass spectrometry approach for global metabolomic profiling and case study on drug-resistant multiple myeloma. *Anal. Chem.* **86**, 3667–3675 (2014).
52. Y. Cyr *et al.*, IMMUNE-RESPONSIVE GENE 1 REGULATES ATHEROSCLEROTIC PLAQUE INFLAMMATION. Gene Expression Omnibus. https://www.ncbi.nlm.nih.gov/geo/query/acc.cgi?acc=GSE252243. Deposited 18 March 2024.